

Revealing the Deposition Mechanism of the Powder Aerosol Deposition Method Using Ceramic Oxide Core–Shell Particles

Mario Linz,* Florian Bühner, Daniel Paulus, Lukas Hennerici, Yiran Guo, Valeriu Mereacre, Ulrich Mansfeld, Martin Seipenbusch, Jaroslaw Kita, and Ralf Moos*

The powder aerosol deposition (PAD) method is a process to manufacture ceramic films completely at room temperature. Since the first reports by Akedo in the late 1990s, much research has been conducted to reveal the exact mechanism of the deposition process. However, it is still not fully understood. This work tackles this challenge using core–shell particles. Two coated oxides, Al_2O_3 core with a SiO_2 shell and $\text{LiNi}_{0.6}\text{Mn}_{0.2}\text{Co}_{0.2}\text{O}_2$ core with a LiNbO_3 shell, are investigated. Initially, the element ratios Al:Si and Ni:Nb of the powder are determined by energy-dispersive X-ray spectroscopy (EDX). In a second step, the change in the element ratios of Al:Si and Ni:Nb after deposition is investigated. The element ratios from powder to film strongly shift toward the shell elements, indicating that the particles fracture and only the outer parts of the particles are deposited. In the last step, this work investigates cross-sections of the deposited films with scanning transmission electron microscopy (STEM combined with EDX and an energy-selective back-scattered electron (EsB) detector to unveil the element distribution within the film itself. Therefore, the following overall picture emerges: particles impact on the substrate or on previously deposited particle, fracture, and only a small part of the impacting particles that originate from the outer part of the impacting particle gets deposited.

(VKS),^[1] vacuum cold spray (VCS),^[2] aerosol deposition method (ADM),^[3] or just aerosol deposition (AD).^[4] A carrier gas aerosolizes the fine, granular powder and a pressure gradient accelerates it through a nozzle into a vacuum chamber.^[5,6] A substrate is mounted in the vacuum chamber where the particles impact at several hundred meters per second, forming a dense ceramic film.^[7] Since the first reports from Akedo et al. in the late 1990's and early 2000's, PAD has become an increasingly widespread tool for different applications and materials.^[8–10] Protective coatings of alumina and yttrium stabilized zirconia (YSZ) against mechanical abrasion or corrosive environments are among the recognized industrial applications.^[11–14] The particle fragments that form the PAD films show a nanocrystalline size with a distorted lattice.^[15] As the numerous grain boundaries and the lattice distortion hinder the electric and ionic conductivity of PAD films, a main focus within the last decades was to improve the quality of these films by a mild thermal annealing.^[16]

1. Introduction

The powder aerosol deposition method (PAD) is a coating process to obtain dense ceramic films. It completely takes place at room temperature. Other terms are vacuum kinetic spray

This affects entire classes of materials and applications such as perovskites for solar cells,^[17,18] oxygen sensing materials such as $\text{Ba}(\text{Fe},\text{Ta})\text{O}_3$ (BFT),^[19,20] and $\text{Sr}(\text{Ti},\text{Fe})\text{O}_3$ (STF),^[21–23] proton ion conductor such as $\text{Ba}(\text{Zr},\text{Y})\text{O}_3$ (BZY)^[24,25] and BaTiO_3 as a piezoelectric material^[26,27] to just name a few of them. Battery

M. Linz, D. Paulus, L. Hennerici, J. Kita, R. Moos
Department of Functional Materials
University of Bayreuth
Universitätsstraße 30, 95447 Bayreuth, Germany
E-mail: funktionsmaterialien@uni-bayreuth.de;
funktionsmaterialien@uni-bayreuth.de

M. Linz, D. Paulus, L. Hennerici, J. Kita, R. Moos
Bayerisches Zentrum für Batterietechnik
Weiherstraße 26, 95448 Bayreuth, Germany
F. Bühner, M. Seipenbusch
Institute of Chemical Process Engineering
University of Stuttgart
70174 Stuttgart, Germany

Y. Guo, V. Mereacre
Institute for Applied Materials – Energy Storage Systems
Karlsruhe Institute of Technology (KIT-IAM-ESS)
76344 Eggenstein-Leopoldshafen, Germany
U. Mansfeld
Bavarian Polymer Institute (BPI)
University of Bayreuth
Universitätsstraße 30, 95447 Bayreuth, Germany

 The ORCID identification number(s) for the author(s) of this article can be found under <https://doi.org/10.1002/adma.202308294>

© 2023 The Authors. Advanced Materials published by Wiley-VCH GmbH. This is an open access article under the terms of the Creative Commons Attribution License, which permits use, distribution and reproduction in any medium, provided the original work is properly cited.

DOI: 10.1002/adma.202308294

materials are also of particular interest for a green and sustainable future: solid-state electrolytes^[28–30] and cathode active materials^[31,32] are well studied. While much work has been directed toward powder synthesis, powder pretreatment,^[34–36] and fluid mechanics of (super-) sonic impinging jets,^[37–39] the deposition mechanism of the PAD has not yet been completely understood. Initially, Akedo suggested the “Room Temperature Impact Consolidation” (RTIC) mechanism, where particles fracture and form an anchor layer.^[40,41] Subsequent particles impact, fragment as well, and consolidate the underlying particles to a dense ceramic film.^[42] This mechanism is also referred to as “hammering effect.”^[43,44] As a direct observation of the impacting and fracturing particles is very difficult, molecular dynamics (MD) simulations could play a key role to investigate the deposition mechanism.^[45] However, results of this study can only be taken into account partially in our study, since the impact of nanoparticles was simulated, and nanoparticles usually get deflected by the stagnation point flow in the real application and cannot reach the substrate at all.^[46–50] Recently, two significant experimental and simulative contributions toward a better understanding were made by Lee et al.^[51] and Furuya et al.^[52] Lee et al.^[51] observed a cushioning effect on ductile substrate materials: particles that hit the ductile substrate first will be less fragmented than those that hit later. Therefore, the ceramic film near the substrate has a lower density (or more voids) than in an area further away from the substrate.^[51] A very interesting observation stems from Furuya et al.^[52] These authors suggested the fragmentation of the impacting particles along a “maximum shear stress line.” A combination of MD simulation and TEM analysis of alumina films could prove a correlation.^[52] The intention of our present study is to shed more light on the deposition mechanism itself. To this end, we used core-shell particles of two different material systems: Al_2O_3 particles with a SiO_2 shell and $\text{LiNi}_{0.6}\text{Mn}_{0.2}\text{Co}_{0.2}\text{O}_2$ particles with a LiNbO_3 shell. Two different material systems were used to obtain more generally valid data. The change in the element ratios between core and shell elements before and after deposition allows us to develop a model of the deposition mechanism. The deposition of core-shell particles by PAD itself has already been demonstrated with the focus of obtaining highly luminescent nanocomposite films.^[33]

2. Experimental Section

In this study, we investigate two material systems: the Al_2O_3 : SiO_2 system and the NMC: LiNbO_3 system. The synthesis of the Al_2O_3 : SiO_2 system was performed as a downstream process with the PAD process directly afterwards, while the NMC: LiNbO_3 coated powder was synthesized according to Mereacre et al.^[53] and were deposited subsequently by the PAD.

To produce Al_2O_3 particles with a SiO_2 shell, a system consisting of an aerosol brush generator, a bubbler system and a tube furnace was used (cf. Figure 1 for the setup). A commercially available Al_2O_3 powder was first sieved with a mesh size of 200 μm and kept dry in an oven at 200 °C to allow for easier deagglomeration in the following process steps. The powder was then fed to an aerosol brush generator, which ensured deagglomeration and aerosolization of the Al_2O_3 particles. The so-formed aerosol was then mixed with tetraethoxysilane (TEOS) enriched nitrogen from a bubbler.^[54] In the next step, high temperature

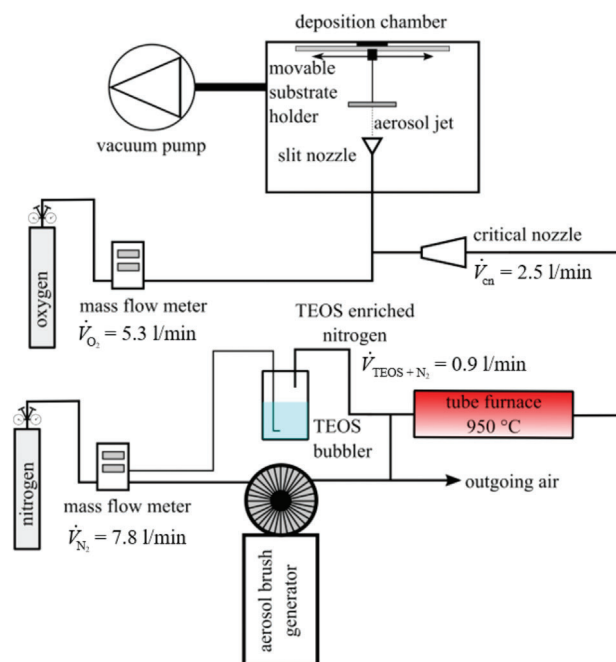


Figure 1. Schematic drawing of the SiO_2 coating of Al_2O_3 particles with the downstream powder aerosol deposition (PAD) apparatus for film manufacturing.

chemical vapor deposition takes place in a tube furnace to deposit the SiO_2 shell onto the Al_2O_3 particles. The system was directly connected to the PAD-apparatus with a critical nozzle to prevent re-agglomeration of the so-formed core-shell particles. This setup ensured a constant flowrate of Al_2O_3 : SiO_2 particles and carrier gas into the low-pressure deposition chamber while keeping the system before the critical nozzle at ambient pressure. To reach sufficiently high impact velocities in the deposition chamber, additional oxygen was added to the flow after the critical nozzle. Impact took place on a stainless steel substrate in this case. Stainless steel (containing Fe and Ni but no Al) was chosen as a substrate material to avoid any interference with the EDX spectra of Al_2O_3 : SiO_2 . The complete setup is schematically depicted in Figure 1 with the respective volume flows of nitrogen and oxygen. Additionally, core-shell particles were collected before entering the deposition chamber, to allow for comparisons of the element ratio of unfragmented particles and particles in the deposited films. As the critical nozzle decouples the pressure and fluid velocity before and after it, a filter was mounted after the critical nozzle and kept the system attached to the vacuum chamber with the vacuum pump. Due to the decoupling of the pressure and the fluid velocity, the reaction and flow conditions in the aerosol generator, bubbler system, and tube furnace remained constant. The powder samples taken were therefore representative for the deposited powder.

The NMC: LiNbO_3 particles were deposited on a Si-wafer using a modified PAD method, the so-called discontinuous PAD (DPAD) process. It was developed to manufacture dense ceramic films with comparable properties as the conventional PAD while using powder quantities less than 100 mg. Oxygen was fed into the gas pressure chamber until 3.7 bar was reached. The ceramic

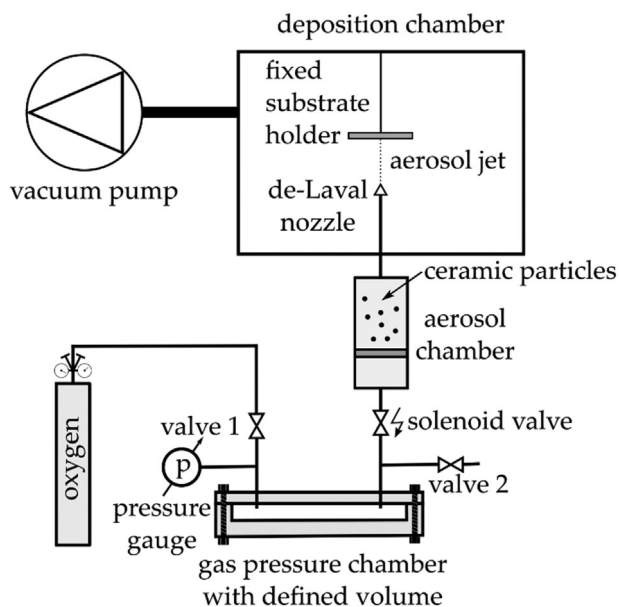


Figure 2. Schematic drawing of the discontinuous powder aerosol deposition (DPAD) apparatus. NMC:LiNbO₃ films were deposited with this setup. Reproduced under the terms of the CC-BY license.^[55] 2021, Linz et al., published by MDPI.

powder was filled into the aerosol chamber and was set under vacuum with the deposition chamber by the vacuum pump. When the solenoid valve was opened, oxygen entrained the ceramic particles, accelerated them, and deposited them as a dense film on the substrate. The details of the apparatus are described in,^[55] while **Figure 2** shows a schematic illustration of it.

NMC:LiNbO₃ core-shell particles were only available in small powder quantities and therefore, the DPAD apparatus was chosen. The synthesis of the core-shell particles is a wet coating process using NMC particles as a starting powder, H₂O₂ as solvent and for chemical activation and a Li/Nb solution for the coating. Subsequent drying and calcination results in the core-shell particles. Further details of the core-shell particle preparation are described in.^[53] Prior to the deposition process, the powders were sieved (sieve mesh size is 200 μm) and stored in a furnace at 200 °C to prevent moisture absorption. A powder quantity of 30–40 mg was filled into the aerosol chamber and subsequently deposited on a Si-wafer. A Si-wafer was chosen as a substrate material, since Si is not present in the NMC:LiNbO₃ film and therefore it does not interfere with the EDX spectrum of the deposited films.

The main analysis of the particles and the films were conducted by SEM imaging (Zeiss Leo 1530, Oberkochen, Germany) and EDX analysis (Thermo Fisher Scientific NS7, Waltham, MA, USA). The particles were dispersed in ethanol and drop-casted on different substrates: stainless steel and carbon substrates for the Al₂O₃:SiO₂ particles and Si-wafers for the NMC:LiNbO₃ particles. A conductive film of carbon (film thickness about 20 nm) was vapor-deposited on top of the particles and the SEM acceleration voltage was chosen to 15 kV. Six to 10 particles per sample are analyzed and the atomic mass of the respective elements were evaluated. The median and the upper and lower quartile was calculated and is shown in **Figure 7**.

A similar procedure was conducted with the ceramic films. A conductive layer of carbon (film thickness about 20 nm) was vapor-deposited on top of the ceramic film and an acceleration voltage of 15 kV was applied. The median of the atomic mass was calculated by measuring different spots on each sample.

To validate the uniformity of the SiO₂ shell for the Al₂O₃:SiO₂ core-shell particles, collected particles were embedded in a resin (Spurr Low Viscosity Embedding Kit, polyscience, USA) and subsequently, thin lamellas were prepared with an ultramicrotome (Leica UCT Ultramicrotome, Wetzlar, Germany) to allow for STEM-EDX analysis of sliced particles.^[56] An analytical 200 kV transmission electron microscope with a field emission gun (JEM-2010F by Jeol, Akishima, Tokyo, Japan) was used to assess the microstructure down to the nanoscale. For analytical studies, the TEM was equipped with an Apollo EDX system from EDAX (Pleasanton, USA). The EDX system was capable of detecting all elements with an atomic number > 11 (sodium). The lower detection limit was about 0.1 wt% and the spatial resolution is about 2 nm. For the STEM (scanning TEM), imaging a probe size of 1 nm was used. Also, a lamella of the Al₂O₃:SiO₂ film was prepared by FIB-SEM (Zeiss Auriga 40 DualBeam, Oberkochen, Germany) for subsequent STEM-EDX mapping of the element composition.

The lamella preparation of the NMC:LiNbO₃ film began with scribing of the Si-wafer using a laser (LPKF ProtoLaser R4, Garbsen, Germany) and subsequent breaking of the substrate into appropriate fragments. The Si-wafer was laser-scribed on the backside, so that the deposited NMC:LiNbO₃ film was not exposed to laser radiation and thus also not to increased temperature. The fragments underwent a wet polishing and a broad ion-milling step with argon ions (Jeol Cryo Ion Slicer, Akishima, Tokyo, Japan). A thinned lamella was investigated in the SEM using an EsB and an EDX detector. The EsB detector provides high-resolution backscattered electron imaging at only 3 kV acceleration voltage. In addition, an energy filtering up to 1.5 keV was applied to obtain only low energy loss electrons close from the surface. The EsB images provide a material contrast image dependent on the average molar mass of the compounds. The large magnification of the images allows for the visualization of the fragmentation of the particles and the distribution of the participating compounds. For EDX analysis the acceleration voltage was set to 15 kV (identical settings as for the analysis of the particles and the films) to investigate the cross-section of the lamella.

3. Results

The collected Al₂O₃:SiO₂ particles were investigated by SEM and STEM. SEM images are shown in **Figure 3**. Parameters in the TEOS bubbler and aerosol brush generator were chosen in a way to ensure an evenly distributed coating and little to no formation of pure SiO₂ particles. **Figure 3a**) shows an overview image and displays agglomerated particles of 2–3 μm in diameter. Little to no pure SiO₂ particles can be detected, which indicates a suitable setting of the bubbler system (TEOS dosing). These particles consist of smaller primary particles of about 300–500 nm and can be seen in **Figure 3b**).

To make sure that the particles were uniformly coated, sliced Al₂O₃:SiO₂ core-shell particles were analyzed by STEM-EDX. The results are shown in **Figure 4**.

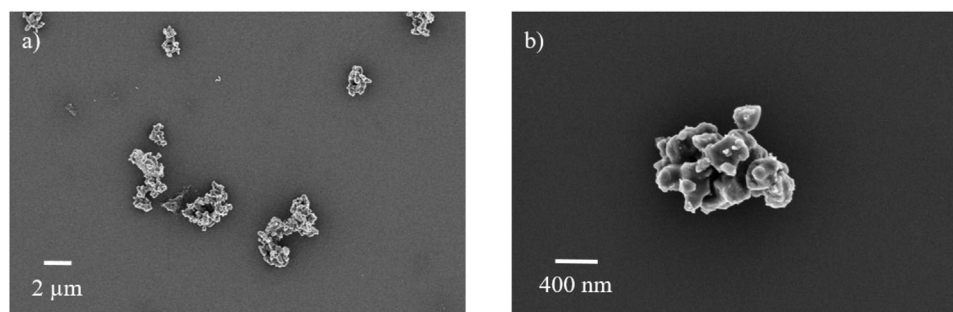


Figure 3. SEM images of the $\text{Al}_2\text{O}_3\text{:SiO}_2$ core-shell particles: Little to no pure SiO_2 particles are generated a) and the coating is evenly distributed b).

The element analysis confirms the formation of a thin and uniform SiO_2 shell around the Al_2O_3 particles (cf. thin blue structure at the edge of the particles in Figure 4b).

SEM images of the NMC:LiNbO_3 particles can be seen in Figure 5. The particles are slightly agglomerated, and they consist of primary particles with diameters of about $2\ \mu\text{m}$ (cf. Figure 5a). The coating is evenly distributed as no inhomogeneities can be found on the particles' surfaces (cf. Figure 5b).

It is possible to manufacture PAD films with both material systems (cf. Figure 6). An example for a PAD film formed by $\text{Al}_2\text{O}_3\text{:SiO}_2$ particles on a stainless steel substrate is shown in Figure 6a). The slit nozzle and the repeated traversing of the substrate results in the rectangular film. A stylus profilometer (Wave-line W20, Jenoptik, Hommel Hercules, Viernheim, Germany) indicates a film thickness of $h_{\text{PAD}} = 150\ \text{nm}$. This sample is used for the continued STEM-EDX analysis. The NMC:LiNbO_3 particles were deposited on a Si-wafer using the DPAD apparatus. The circular shaped film (cf. Figure 6b) results from the circular de-Laval nozzle. It is difficult to determine the maximum height of the Gaussian shaped film profile with a stylus profilometer.^[55] The smooth transition from substrate to film, the small inclination angle from the edge of the film to the maximum and the surface roughness of the film affect the measurements. Nevertheless, the film thickness of the NMC:LiNbO_3 system could be determined to $h_{\text{DPAD}} = 500\ \text{nm}$ by using the EsB image of the cross-section (cf. Figure 11).

A quantitative analysis of the element distribution between shell elements and core elements of the particles and the films was performed by standardless quantification from SEM-EDX normal to the coated surface. Substrate materials were chosen so

that they do not interfere in the energy spectrum with elements of core and shell. Several particles from each sample were investigated and the atomic percentage was calculated from the K-line of Si ($K_{\alpha} = 1.74\ \text{keV}$) and Al ($K_{\alpha} = 1.49\ \text{keV}$). In total, 11 different positions on four different powder samples were investigated for $\text{Al}_2\text{O}_3\text{:SiO}_2$ particles. The $\text{Al}_2\text{O}_3\text{:SiO}_2$ film was analyzed on two different areas from one sample. The analyzed area of the film was $665\ \mu\text{m}^2$. For each particle, the atomic percentage of Si was divided by the atomic percentage of the Al. The median of all particles is displayed in Figure 7 with error bars that represent the upper and lower quartile of the median. The preparation and evaluation steps for the NMC:LiNbO_3 particles vary as a Si-wafer is chosen as substrate material and the Nb L-line ($L_{\alpha 1} = 2.17\ \text{keV}$) and Ni K-line ($K_{\alpha 1} = 7.48\ \text{keV}$) was used to determine the atomic percentage and therefore the element ratio. In total, eight different positions on two different powder samples were investigated for NMC:LiNbO_3 particles. The NMC:LiNbO_3 film was analyzed on four different areas from one sample. The analyzed area of the film was about $32600\ \mu\text{m}^2$.

The atomic percentage of the $\text{Al}_2\text{O}_3\text{:SiO}_2$ films and the NMC:LiNbO_3 films were calculated analogously to the previous procedure. The median, the upper and the lower quartile (plotted as error bars) were determined as different areas on the respective sample were evaluated. The results are plotted in Figure 7.

In the particles of both material systems, core elements (Al and Ni respectively) and shell elements (Si and Nb respectively) are detectable. The medians of the particle element ratios are $\text{Si:Al} = 0.23$ and $\text{Nb:Ni} = 0.07$. After deposition, the medians of the films show a significant increase in shell elements: $\text{Si:Al} = 0.39$ and $\text{Nb:Ni} = 0.64$. Regardless of the increase in shell elements, core

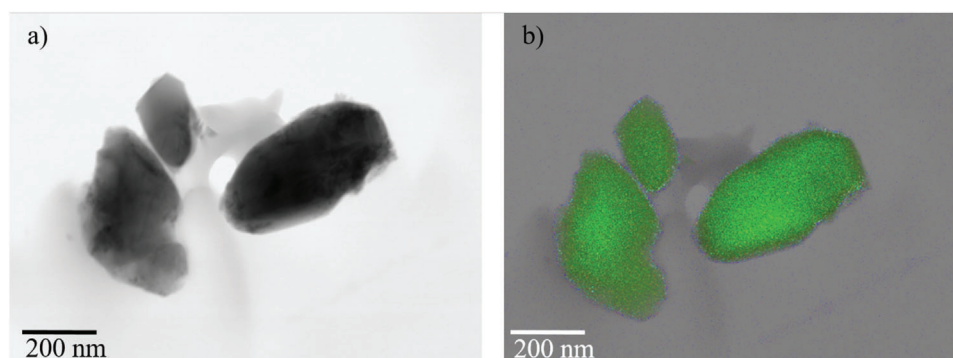


Figure 4. a) STEM image of sliced $\text{Al}_2\text{O}_3\text{:SiO}_2$ core-shell particles. b) EDX analysis of element distribution (green = Al, blue = Si, red = O)

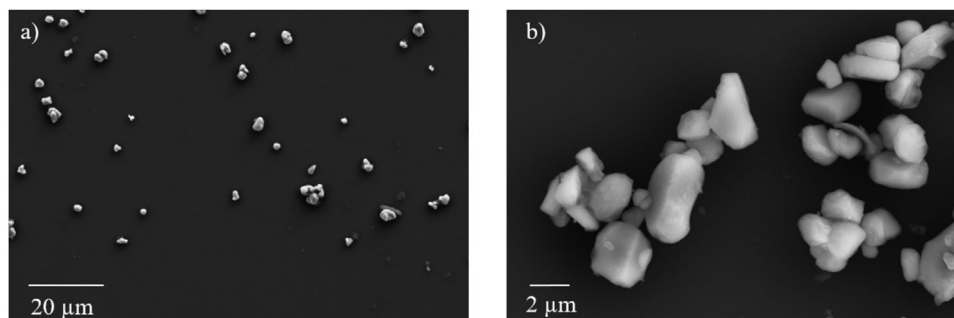


Figure 5. SEM images of the NMC:LiNbO₃ particles on a Si-wafer as a substrate. a,b) The images show different spots of the sample in different magnifications. The particles are slightly agglomerated and they are composed of primary particles with a diameter of approximately 2 μm.

elements can still be detected in the film. Although, a minor error in quantification due to geometry differences and the heterogenic nature of core-shell particles cannot be excluded, this is an indication that only a part of the particle (namely mainly the outer part) is deposited in the film, since otherwise the element ratio before and after deposition would be similar. By the presence of core elements in the film, we can also exclude that only the shell or even more only parts of the shell are deposited. Subsequently,

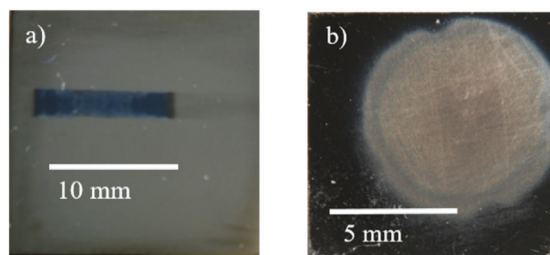


Figure 6. Comparison of the deposited powder aerosol deposition (PAD) films: The Al₂O₃:SiO₂ system is deposited by conventional PAD a) (dark, rectangular film; stainless steel substrate) and the NMC:LiNbO₃ system by discontinuous PAD (DPAD) b) (bright, round film; Si-wafer as substrate).

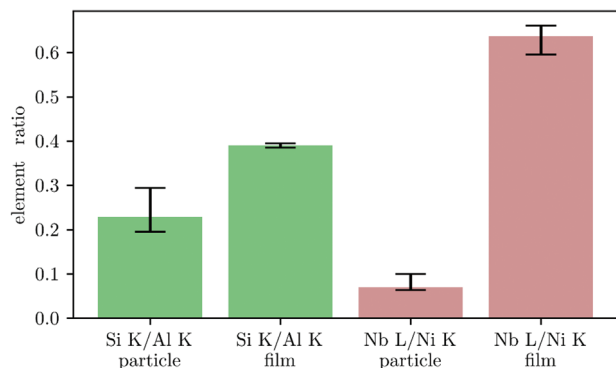


Figure 7. Comparison of the standardless EDX quantification of the SiO₂:Al₂O₃ system and the NMC:LiNbO₃ system. Both material systems show a shift in the element ratio (atomic ratio) toward the shell elements (Si and Nb respectively) in the deposited state (film). Nevertheless, core material (Al and Ni respectively) can be detected in the film. The bars are the median of the ratio of the weight percentage of the respective elements. The error bars represent the upper and lower quartile of the respective medians.

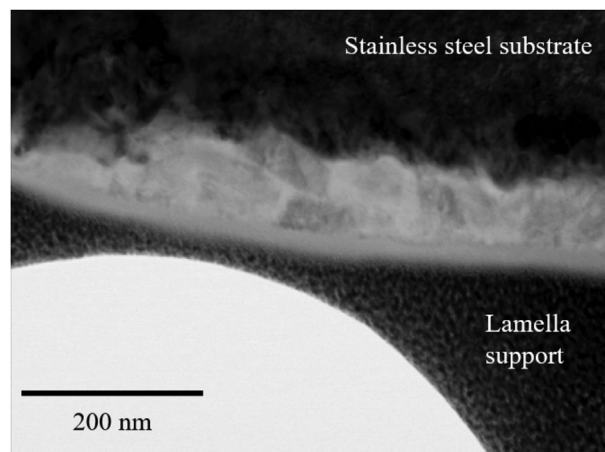


Figure 8. STEM image of an Al₂O₃:SiO₂ film on a stainless steel substrate.

lamellae of the respective films are evaluated by STEM-EDX and EsB to support the partial deposition of the particles.

Figure 8 shows an STEM image of a thin lamella that was prepared from the Al₂O₃:SiO₂ film. Contrast differences in the nanocrystalline film verify the fragmentation of the primary particles.

The element composition of the Al₂O₃:SiO₂ lamella was subsequently investigated with STEM-EDX mapping, as can be seen in **Figure 9**. Green color relates to aluminum, purple to silicon, and red to oxygen. Accumulation of SiO₂ between larger Al₂O₃ fragments can clearly be observed. The different size of the particles before (2–3 μm agglomerated particles with primary particles

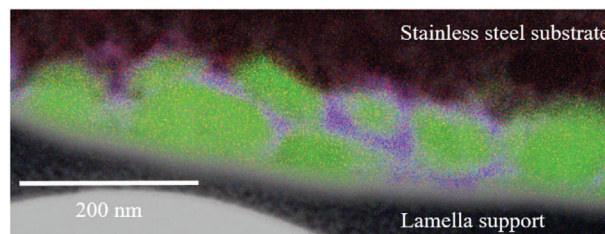


Figure 9. STEM-EDX mapping of an Al₂O₃:SiO₂ film. The colors indicate the following elements: green relates to aluminum, purple to silicon, and red to oxygen.

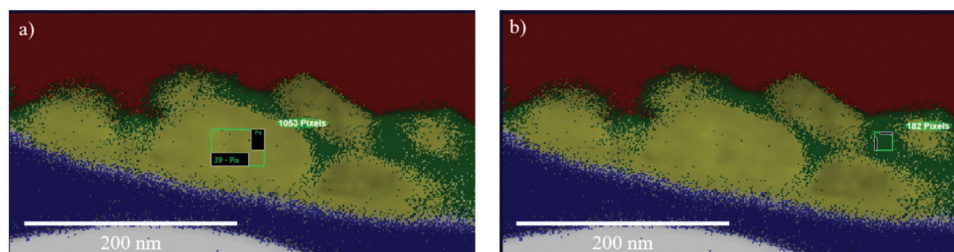


Figure 10. STEM–EDX image at $\text{Al}_2\text{O}_3:\text{SiO}_2$ films with a color-indicating element composition. Two areas are analyzed respectively. a) The evaluation area of the aluminum-rich area and b) the silicon-rich area.

of about 500 nm, cf. Figure 3b) and after deposition (fragments of 50–100 nm, cf. Figure 9) points unambiguously to a fragmentation process as it is typical for PAD. From Figure 9, the area fraction of Si and Al can be determined. This results in the respective areas of $\text{Al}_2\text{O}_3 = 24450.25 \text{ px}^2$ and $\text{SiO}_2 = 9232.36 \text{ px}^2$ (for details, please see Figure S1, Supporting Information). The ratio of the two areas $A_{\text{SiO}_2}/A_{\text{Al}_2\text{O}_3} = 0.38$ almost matches the standardless EDX quantification $\text{Si}:\text{Al} = 0.39$ (cf. Figure 7) of the deposited $\text{Al}_2\text{O}_3:\text{SiO}_2$ film. The quantification of nanocrystalline films on a single TEM lamella is of course always subject to uncertainties. Nevertheless, the tendency that a higher shell fraction is deposited can be confirmed.

This further supports the results obtained by the quantitative EDX measurements of particles and films normal to the surface conducted earlier. Small areas of this lamella were investigated further regarding element composition: aluminum-rich (cf. Figure 10a) and silicon-rich (cf. Figure 10b) areas were investigated respectively.

Here, yellow indicates aluminum while dark green indicates silicon. The calculated element ratios are $\text{Si}:\text{Al} = 1.2 \times 10^{-3}$ in the aluminum-rich area (cf. Figure 10a) and $\text{Si}:\text{Al} = 6.2$ in the silicon-rich area (cf. Figure 10b). The element ratios in the respective regions differ by three orders of magnitude and show that the aluminum-rich region is almost exclusively alumina and the silicon-rich region is almost exclusively silica.

The NMC: LiNbO_3 particles were deposited on a Si-wafer. An EsB image of the film is shown in Figure 11. The EsB is sen-

sitive to the average atomic mass, so Si (black, substrate), carbon (black, contamination within the darker gray and whitish areas), NMC (darker gray, core material), and LiNbO_3 (whitish, shell material) are represented by contrast. The particles before deposition (cf. Figure 5) have a diameter of about 2 μm . While one significantly large fragment of NMC (diameter is about 500 nm) can be observed, all other fragments of NMC are in the range of 100 nm or less. Furthermore, the NMC particles are well surrounded by LiNbO_3 , indicated by the whitish structures. Figure 11 supports the EDX data from the results shown in Figure 7, where the element ratio of the film is determined to $\text{Nb}:\text{Ni} = 0.64$. Much more whitish structures (Nb) can be found in the film as initially expected from the particles ($\text{Nb}:\text{Ni} = 0.07$). If we count the number of pixels of the area that is assigned to LiNbO_3 (whitish structures: $\text{LiNbO}_3 = 68400 \text{ px}^2$) and NMC (darker, grayish structures: $A_{\text{NMC}} = 97300 \text{ px}^2$) respectively, we obtain an area ratio of about $\text{LiNbO}_3/\text{NMC} = 0.7$. The discrepancy between standardless EDX measurement and counted pixels may vary depending on where the TEM lamella is cut. Shifting the cut in a nanocrystalline layer can result in smaller deviations in irregular structures. Nevertheless, a significant shift toward shell material can clearly be observed. For details of the counted pixels, please see Figure S2 (Supporting Information).

In addition to the EsB measurements, the lamellas were also investigated by SEM–EDX. The results are shown in Figure 12. Figure 12a is the grayscale image of the coating and Figure 12b

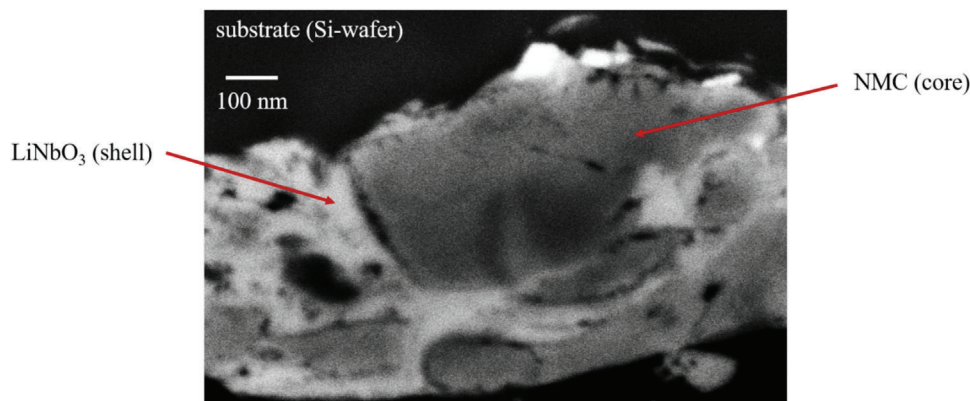


Figure 11. EsB image of a cross section of an NMC: LiNbO_3 film. The darker grayish structures represent the NMC (core material) while the whitish structures correspond to the LiNbO_3 (shell material). The film is deposited on a Si-wafer (substrate material, black in the upper part of the image). The fragmentation into nanocrystalline fragments can be clearly observed. An increase of shell material is also visible.

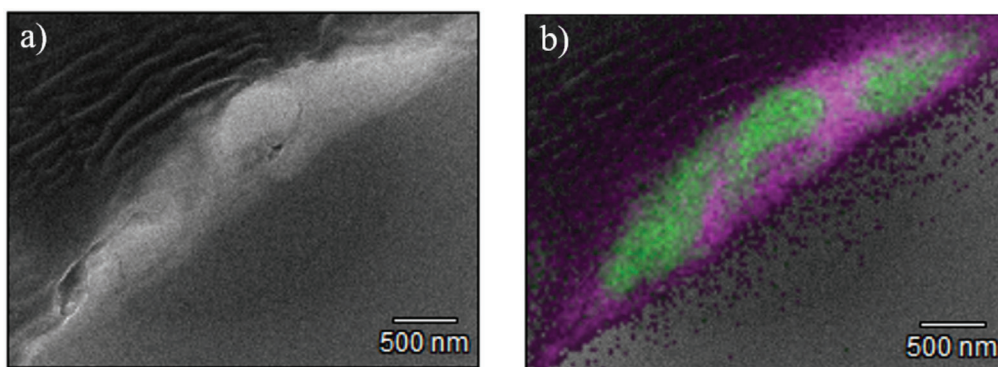


Figure 12. EDX-mapping of a cross-section of an NMC:LiNbO₃ film. The grayscale image a) shows the cross-section. The core element Ni (green) and the shell element Nb (pink) are shown as an overlay with the grayscale image in (b). Areas with a high Ni count show a lack of Nb and vice versa. The areas of core and shell elements can be clearly distinguished.

represents the EDX-mapping as an overlay of the grayscale image. The core element Ni is represented by green color, while pink indicates the shell element Nb. The substrate material (Si-wafer) is on the right lower corner, while the upper left corner shows epoxy resin from the ion beam milling process on the surface of the lamella (view into the depth). EDX measurements clearly exhibit the presence of core (Ni, green color) and shell (Nb, pink color) elements. Once again, the size of the observable fragments is smaller than the initial particles, indicating a frac-

ture mechanism that they must have undergone to form a dense film.

According to the results of the Al₂O₃:SiO₂ system and the NMC:LiNbO₃ system, we developed a qualitative model to explain the film formation during the deposition from a mechanistic standpoint. It is illustrated in **Figure 13**. The element ratio of the particles before deposition was examined by EDX and indicate a high amount of the core elements and a low amount of shell elements (cf. Figure 13a). The core-shell

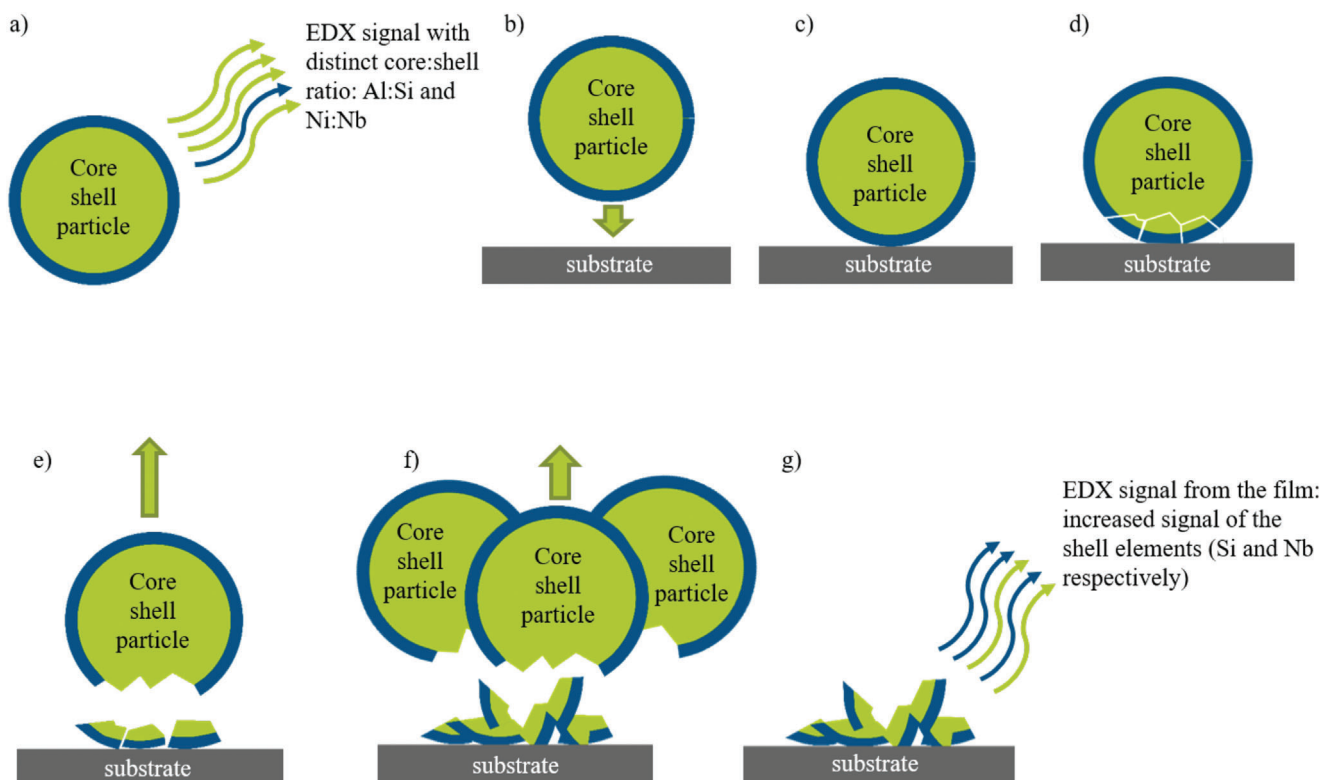


Figure 13. Initially, the element ratio between core and shell is determined by EDX before spraying (a). The particles are accelerated by the gas flow toward the substrate (b) and impact at the substrate (c). The particle fragment (d) and a part of the shell as well as a part of the core is deposited. Subsequent particles undergo the same process and form the film. The final film is characterized by EDX (g) whereas a significantly more deposited shell material can be determined.

particles are accelerated toward the substrate (Figure 13b) and impact on the substrate (Figure 13c). The particles fracture from about 2 μm (initial particle size before deposition, cf. Figures 3 and 5) to fragments of about 200 nm (cf. Figures 9 and 11). Only parts of the particles are deposited (Figure 13e), otherwise, the increase of the share of the shell elements (as indicated by EDX, cf. Figure 7) cannot be explained. The remaining parts of the particles follow with the gas flow toward the vacuum pump. It is uncertain whether the remaining parts of the particles will break as well. These results support the findings of Furuya et al.,^[52] suggesting that particles fracture along a “maximum shear stress line.” Subsequent particles impact and contribute to the film growth (Figure 13f). The EDX analysis after deposition (Figure 13g) shows the increase of the shell elements within the film.

4. Conclusions

In this work, we developed a model to explain the deposition mechanism of the PAD based on experimental results. To achieve this, we investigated the different element compositions of core-shell particles by EDX prior to deposition and after film formation. Two different material systems, Al_2O_3 with a SiO_2 coating ($\text{Al}_2\text{O}_3:\text{SiO}_2$ system) and NMC with a LiNbO_3 coating (NMC: LiNbO_3 system) were deposited, examined, and compared. For both material systems, we initially measured the element ratios of the shell and the core elements of the powders ($\text{Si}:\text{Al} = 0.23$ and $\text{Nb}:\text{Ni} = 0.07$ respectively). After deposition, both material systems show an increased amount of the shell elements ($\text{Si}:\text{Al} = 0.39$ and $\text{Nb}:\text{Ni} = 0.64$, respectively). Nevertheless, a certain amount of the core element can still be observed after deposition. A complete deposition of the entire particle or a sole deposition of the shell can be negated: for these cases, either the element ratios prior and after deposition must have remained constant or only shell elements should be detectable. A shift toward an increasing amount of shell elements can only be explained by a partial deposition of the impacting particles. A further investigation by STEM-EDX ($\text{Al}_2\text{O}_3:\text{SiO}_2$ system), EsB, and EDX (both NMC: LiNbO_3 system) of cross-section lamellae confirm the deposition mechanism. Both material systems show fragments of the initial particles with a high amount of shell elements. Therefore, we conclude that particles impact, fracture, and only a small part originating from the outer part of the impacting particle is deposited. These results are also consistent with those of Furuya et al.,^[52] who propose a maximum shear stress line as the fracture edge through the particles.

Based on this work, two particularly interesting questions arise for the future: does the elemental shift toward shell material persist with significantly thicker films than the anchor layer, and can the behavior be reproduced with a reversed core-shell element composition? The cushioning effect discussed by Lee et al.^[51] along with the impact of varying hardness through the reversal of core and shell elements, could provide additional understanding of the interactions between the substrate, film, and impacting particles. Moreover, further experiments with other ceramic oxide core-shell materials should be conducted to provide additional evidence for the generality of the proposed mechanism.

Supporting Information

Supporting Information is available from the Wiley Online Library or from the author.

Acknowledgements

The authors would like to thank the German Research Foundation (DFG) for funding (DFG Grant MO 1060/40-1). Equal thanks go to the Federal Ministry of Education and Research (BMBF) in the framework of the Fest-Batt2 cluster (BMBF Grants 03XP0441A and 03XP0433A) and the Bavarian Center for Battery Technology (BayBatt) for funding this research work. The authors thank M. Heider from the Bayreuth Institute of Macromolecular Research (BIMF) for taking SEM images and acquiring EDX data. Equal thanks go to M. Schwarzmann (Chair of Inorganic Colloids for Electrochemical Energy Storage—Professor Dr. Josef Breu) for the preparation of the TEM lamellae for the NMC: LiNbO_3 system. The authors would also like to thank the Bavarian Polymer Institute (BPI, Keylab Electron and Optical Microscopy) for providing the SEM and ion milling instruments. The authors also gratefully acknowledge the core facility SRF AMICA (Stuttgart Research Focus Advanced Materials Innovation and Characterization) at the University of Stuttgart for their support and assistance in this work. In this regard, special thanks go to M. Schweikert for preparing the sliced particles, D. Willer for preparing the TEM lamella, and F. Kauffmann for conducting the STEM-EDX analysis of the $\text{Al}_2\text{O}_3:\text{SiO}_2$ system.

Open access funding enabled and organized by Projekt DEAL.

Conflict of Interest

The authors declare no conflict of interest.

Author Contributions

M.L. and F.B. contributed equally to this work. M.L. and F.B. conceived the setup, conducted the experiments, and evaluated the results. The NMC: LiNbO_3 core-shell particles were provided by Y.G. and V.M. M.L. and U.M. conducted the SEM imaging and EDX measurements. All authors discussed the received results. L.H. and D.P. contributed with their specific knowledge of the PAD apparatus. J.K. and R.M. supervised the work, while M.S. and R.M. carried out the project. M.L., F.B., and R.M. wrote the paper. All authors have read and agreed to the published version of the manuscript.

Data Availability Statement

The data that support the findings of this study are available in the Supporting Information material of this article.

Keywords

core-shell particles, deposition mechanism, powder aerosol deposition method (PAD), room-temperature impact consolidation (RTIC), vacuum kinetic spray (VKS)

Received: August 16, 2023

Revised: October 3, 2023

Published online:

[1] H. Kwon, Y. Kim, H. Park, C. Lee, *Surf. Coat. Technol.* **2019**, 374, 493.

- [2] L.-S. Wang, H.-F. Zhou, K.-J. Zhang, Y.-Y. Wang, C.-X. Li, X.-T. Luo, G.-J. Yang, C.-J. Li, *Ceram. Int.* **2016**, *43*, 4390.
- [3] D. Hanft, J. Exner, M. Schubert, T. Stöcker, P. Fuierer, R. Moos, *J. Ceram. Sci. Technol.* **2015**, *6*, 147.
- [4] J. Exner, M. Hahn, M. Schubert, D. Hanft, P. Fuierer, R. Moos, *Adv. Powder Technol.* **2015**, *26*, 1143.
- [5] M. Schubert, J. Exner, R. Moos, *Materials* **2014**, *7*, 5633.
- [6] J. Akedo, M. Lebedev, *Jpn. J. Appl. Phys.* **2001**, *40*, 5528.
- [7] M. W. Lee, J. J. Park, D. Y. Kim, S. S. Yoon, H. Y. Kim, D. H. Kim, S. C. James, S. Chandra, T. Coyle, J. H. Ryu, W. H. Yoon, D. S. Park, *J. Aerosol Sci.* **2011**, *42*, 771.
- [8] J. Akedo, M. Lebedev, *Jpn. J. Appl. Phys.* **1999**, *38*, 5397.
- [9] J. Akedo, M. Lebedev, *Appl. Phys. Lett.* **2000**, *77*, 1710.
- [10] J. Akedo, M. Lebedev, *Jpn. J. Appl. Phys.* **2002**, *41*, 6980.
- [11] H. Choi, K. Kim, H. Choi, S. Kang, J. Yun, Y. Shin, T. Kim, *Surf. Coat. Technol.* **2010**, *205*, S125.
- [12] J. Iwasawa, R. Nishimizu, M. Tokita, M. Kiyohara, K. Uematsu, *J. Am. Ceram. Soc.* **2007**, *90*, 2327.
- [13] H. S. Ryu, T. S. Lim, J. Ryu, S.-H. Hong, *J. Electrochem. Soc.* **2012**, *160*, C42.
- [14] N. Seto, K. Endo, N. Sakamoto, S. Hirose, J. Akedo, *J. Therm. Spray Technol.* **2014**, *23*, 1373.
- [15] F. Cao, H. Park, J. Heo, J. Kwon, C. Lee, *J. Therm. Spray Technol.* **2013**, *22*, 1109.
- [16] J. Exner, T. Nazarenus, D. Hanft, J. Kita, R. Moos, *Adv. Mater.* **2020**, *32*, 1908104.
- [17] F. Panzer, D. Hanft, T. Gujar, F.-J. Kahle, M. Thelakkat, A. Köhler, R. Moos, *Materials* **2016**, *9*, 277.
- [18] N. Leupold, A. L. Seibel, R. Moos, F. Panzer, *Eur. J. Inorg. Chem.* **2021**, *2021*, 2882.
- [19] M. Bektas, D. Hanft, D. Schönauer-Kamin, T. Stöcker, G. Hagen, R. Moos, *J. Sens. Sens. Syst.* **2014**, *3*, 223.
- [20] M. Bektas, T. Stöcker, A. Mergner, G. Hagen, R. Moos, *J. Sens. Sens. Syst.* **2018**, *7*, 289.
- [21] D. Popovici, H. Tsuda, J. Akedo, *J. Appl. Phys.* **2009**, *105*, 61638.
- [22] R. Moos, N. Izu, F. Rettig, S. Reiß, W. Shin, I. Matsubara, *Sensors* **2011**, *11*, 3439.
- [23] J. Exner, M. Schubert, D. Hanft, T. Stöcker, P. Fuierer, R. Moos, *Sens. Actuators, B* **2016**, *230*, 427.
- [24] J. Exner, T. Nazarenus, J. Kita, R. Moos, *Int. J. Hydrogen Energy* **2020**, *45*, 10000.
- [25] H. Bae, J. Choi, K. J. Kim, D. Park, G. M. Choi, *Int. J. Hydrogen Energy* **2015**, *40*, 2775.
- [26] N. H. Khansur, U. Eckstein, L. Benker, U. Deisinger, B. Merle, K. G. Webber, *Ceram. Int.* **2018**, *44*, 16295.
- [27] D. R. Patil, V. Annapureddy, J. Kaarthik, A. Thakre, J. Akedo, J. Ryu, *Actuators* **2020**, *9*, 59.
- [28] R. Inada, T. Okada, A. Bando, T. Tojo, Y. Sakurai, *Prog. Nat. Sci.: Mater. Int.* **2017**, *27*, 350.
- [29] D. Hanft, J. Exner, R. Moos, *J. Power Sources* **2017**, *361*, 61.
- [30] M. Shoji, E. J. Cheng, T. Kimura, K. Kanamura, *J. Phys. D: Appl. Phys.* **2019**, *52*, 103001.
- [31] M. Sakakura, Y. Iriyama, *J. Asian Ceram. Soc.* **2022**.
- [32] E. J. Cheng, R. Oyama, T. Abe, K. Kanamura, *J. Eur. Ceram. Soc.* **2023**, *43*, 2033.
- [33] S. Kim, M.-Y. Cho, I.-S. Kim, W.-J. Kim, S.-H. Park, S. Baek, J.-M. Oh, S.-W. Kim, *Adv. Mater. Interfaces* **2019**, *6*, 1900359.
- [34] J. Exner, M. Schubert, D. Hanft, J. Kita, R. Moos, *J. Eur. Ceram. Soc.* **2019**, *39*, 592.
- [35] K. Mihara, T. Hoshina, H. Kakemoto, H. Takeda, T. Tsurumi, *Key Eng. Mater.* **2009**, 421–422, 165.
- [36] D.-W. Lee, H.-J. Kim, S.-M. Nam, *J. Korean Phys. Soc.* **2010**, *57*, 1115.
- [37] B. Farahani, M. Jadidi, S. Moghtadernejad, *Coatings* **2022**, *12*, 1578.
- [38] R. Saunders, S. D. Johnson, D. Schwer, E. A. Patterson, H. Ryou, E. P. Gorzkowski, *J. Therm. Spray Technol.* **2021**, *30*, 523.
- [39] H. Park, H. Kwon, Y. Kim, C. Lee, *J. Therm. Spray Technol.* **2019**, *17*, 181.
- [40] J. Akedo, *J. Am. Ceram. Soc.* **2006**, *89*, 1834.
- [41] J. Akedo, *J. Ceram. Soc. Jpn.* **2020**, *128*, 101.
- [42] J. Akedo, *J. Therm. Spray Technol.* **2008**, *17*, 181.
- [43] D.-W. Lee, H.-J. Kim, Y.-H. Kim, Y.-H. Yun, S.-M. Nam, *J. Am. Ceram. Soc.* **2011**, *94*, 3131.
- [44] H. Park, J. Kwon, I. Lee, C. Lee, *Scr. Mater.* **2015**, *100*, 44.
- [45] B. Daneshian, F. Gärtner, H. Assadi, M. V. Vidaller, D. Höche, T. Klassen, *Surf. Coat. Technol.* **2022**, *429*, 127886.
- [46] H. Ogawa, *Mater. Trans.* **2005**, *46*, 1235.
- [47] H. Ogawa, *Mater. Trans.* **2006**, *47*, 1945.
- [48] H. Ogawa, *Mater. Trans.* **2007**, *48*, 2067.
- [49] P. Sarobol, M. Chandross, J. D. Carroll, W. M. Mook, D. C. Bufford, B. L. Boyce, K. Hattar, P. G. Kotula, A. C. Hall, *J. Therm. Spray Technol.* **2016**, *25*, 82.
- [50] H.-L. Yao, G.-J. Yang, C.-J. Li, *J. Nanosci. Nanotechnol.* **2018**, *18*, 2657.
- [51] C. Lee, M.-Y. Cho, M. Kim, J. Jang, Y. Oh, K. Oh, S. Kim, B. Park, B. Kim, S.-M. Koo, J.-M. Oh, D. Lee, *Sci. Rep.* **2019**, *9*, 2166.
- [52] Y. Furuya, S. Konuma, M. Hasegawa, *Surf. Coat. Technol.* **2023**, *458*, 129362.
- [53] V. Mereacre, P. Stübke, A. Ghamlouché, J. R. Binder, *Nanomaterials* **2021**, *11*, 548.
- [54] P. Post, L. Wurlitzer, W. Maus-Friedrichs, A. P. Weber, *Nanomaterials* **2018**, *8*, 530.
- [55] M. Linz, J. Exner, J. Kita, F. Bühner, M. Seipenbusch, R. Moos, *Coatings* **2021**, *11*, 844.
- [56] A. R. Spurr, *J. Ultrastruct. Res.* **1969**, *26*, 31.